13th International Symposium on Turbulence and Shear Flow Phenomena (TSFP13)
Montreal, Canada, June 25–28, 2024

DIRECT NUMERICAL SIMULATION OF UNSTEADY BOUNDARY-LAYER SEPARATION IN A COMPRESSOR CASCADE

Taiyang Wang
HEDPS, Center for Applied Physics and Technology
College of Engineering, Peking University
Beijing 100871, China
wangtaiyang@stu.pku.edu.cn

Yaomin Zhao
HEDPS, Center for Applied Physics and Technology
College of Engineering, Peking University
Beijing 100871, China
yaomin.zhao@pku.edu.cn

ABSTRACT

Direct numerical simulations (DNS) have been conducted to analyze the flow within a compressor cascade, where both the suction-side and pressure-side boundary layers exhibit unsteady separation phenomena. The current investigation primarily focuses on the frequency characteristics, exploring hydrodynamic instabilities and acoustic features. Identified with dynamic mode decomposition (DMD) analysis, the laminar (case L) and turbulent (case T) scenarios present different dominant frequencies. Based on classical linear stability analysis (LSA) and forced Navier-Stokes simulations (Jones *et al.*, 2010), it has been observed that the dominant frequencies are mainly affected by suction-side events. Moreover, case L appears to be under the control of an acoustic feedback loop and near-wake instability, whereas case T is probably impacted by inviscid inflectional instabilities. Additionally, the pressure-side boundary layer likely experiences the influence of scattered waves originating from the suction side. Furthermore, the dissimilar frequency responses of case T are attributed to the self-sustaining turbulence due to the mode-B instability.

INTRODUCTION

In light of adverse pressure gradients, the compressor boundary layers frequently exhibit unsteady separated flows (Zaki *et al.*, 2010), leading to an increase in kinetic losses (Sandberg & Michelassi, 2022). Consequently, predicting the frequency response of the unsteady separation proves invaluable for optimizing separation control strategies. Moreover, aerofoils experiencing unsteady separation may result in tonal noise emissions, which are particularly unwanted. Therefore, gaining deeper insights into the mechanisms driving noise generation can facilitate the development of effective strategies for noise elimination (Pröbsting *et al.*, 2015). Nonetheless, the intricate interplay between various hydrodynamic instability mechanisms and acoustic behaviours is still ambiguous, requiring further elucidation.

Characterized by the superposition of multiple secondary tones f_n $(n = 1, 2, \cdots)$ and a dominant tone $f_{n_{\max}}$, the acoustic spectrum of tonal noise reveals a ladder-type pattern (Paterson *et al.*, 1973). In order to make clear these phenomena, Paterson *et al.* (1973) drew an analogy with the wake shedding of a bluff body, but failed to explain secondary tones. Based on the acoustic feedback model pitched by Tam (1974), the ladder-like structure can be qualitatively explained, whereas the average evolution of $f_{n_{\max}}$ is not account for. Subsequently, Fink (1975) put forward an unstable boundary-layer model and posited that $f_{n_{\max}}$ is instigated by Tollmien–Schlichting instabilities from upstream. Nevertheless, no experiment was conducted to support the assertion. Afterwards, Longhouse (1977) argued that the receptivity region of the feedback resides within the boundary layer rather than in the wake region as proposed by Paterson *et al.* (1973). Conversely, Arbey & Bataille (1983) pointed out that the feedback stems from the maximum velocity point on the aerofoil. Besides, it was observed that $f_{n_{\max}}$ closely aligns with the broadband center frequency f_s, which can be estimated by

$$f_s \approx 0.011 \frac{U_\infty^{3/2}}{(c\nu_\infty)^{1/2}}. \tag{1}$$

Additionally, denoting the length of the feedback loop as L, f_n can be derived incorporating the phase relationship

$$f_n = \frac{1}{L}\left(n + \frac{1}{2}\right) \frac{1}{1/c_r + 1/(c_\infty - U_\infty)}. \tag{2}$$

Here, c_r and c_∞ are the phase velocities of unstable and acoustic waves, respectively.

Although the revised acoustic feedback model has provided satisfactory explanation on secondary tones, the determining factor of dominant frequency remains open. Initially ascribed solely to boundary layer instability, the selection of the dominant frequency has been linked to various factors ranging from the Kelvin–Helmholtz instability within detached shear layers (Pauley *et al.*, 1990) to inviscid Rayleigh inflectional instabilities (Desquesnes *et al.*, 2007), chosen based on their highest total amplification rates. Nevertheless, local stability analysis on boundary layers does not always lead to an accurate

estimation (Jones *et al.*, 2008), prompting subsequent studies to propose that the dominant frequency is predominantly determined by the absolute instability of the laminar wake (Ikeda *et al.*, 2012; Tam & Ju, 2012). However, the absence of secondary frequencies has hindered the widespread acceptance of these findings. In contrast to the localized perspective, Jones *et al.* (2010) introduced a global mechanism, noting that the frequency contents of the initial wave-packet tend to converge towards the vortex shedding frequency following several feedback-loop cycles.

In addition, some controversies still exist on the concrete process of acoustic feedback loop, especially the respective significance of pressure- and suction-side events, along with their interaction. Experiments conducted by Nash *et al.* (1999) indicated that acoustic tones primarily stemmed from pressure-side boundary layer instabilities, while Jones *et al.* (2010) claimed that feedback occurred purely on the suction side. Apart from pressure-side events, Desquesnes *et al.* (2007) proposed a secondary feedback loop existed on the suction side. Subsequent studies clarified that tonal noise generation is dominated by suction-side events at low Reynolds number and shifts towards pressure-side events at high Reynolds number (Pröbsting *et al.*, 2015). Afterwards, Arcondoulis *et al.* (2019) proposed a dual acoustic feedback model, where feedback acted independently on the pressure and suction surfaces.

The above-mentioned studies underscore the substantial influence of boundary layers attributes on tonal noise production, suggesting that more abundant separation phenomena in compressor cascades may yield more intricate findings. Nonetheless, the realization of a highly resolved DNS for compressor cascades became feasible not until a dozen years ago due to computational constraints (Zaki *et al.*, 2010), with earlier studies predominantly centered on transition mechanisms (Mao *et al.*, 2017).

In the present study, employing multiple analytical approaches, we investigate the mechanisms responsible for the frequency response in the flows of compressor cascades, focusing on the effects of both hydrodynamic and acoustic instabilities.

METHODOLOGY

Direct numerical simulation

Two three-dimensional DNSs are performed to explicate the fluid dynamics within a linear compressor cascade, and the inlet Mach number is $Ma = 0.15$ and the axial Reynolds number is $Re_c = 138,500$. In the absence of external perturbations, one simulation is labeled as case L, representing a laminar flow. For comparison, case T is initiated from case L but with an extra small-amplitude stochastic disturbance imposed only at the first time step, and it undergoes a laminar-turbulent transition in the suction-side boundary layer.

The non-dimensionalized three-dimensional compressible Navier–Stokes equations in a conservative form

$$\frac{\partial}{\partial t}Q_i + \frac{\partial}{\partial x_j}(E_{ji} - F_{ji}) = 0 \tag{3}$$

are solved by the high-order finite difference solver HiPSTAR (Sandberg *et al.*, 2015). Here, the index i represents a free variable, whereas $j = 1, 2, 3$ serve as a dummy variable indicating three spatial dimensions. Besides, Q_i, E_{ji} and F_{ji} are conservative variable vectors, inviscid and viscous fluxes, respectively.

Dynamic mode decomposition

As a generalization of global instability analysis, DMD has potential to elucidate the global behaviour of the overall flow, whereas requiring much smaller computational resources (Schmid, 2010).

Concentrating on the time-resolved flow field within the boundary layers, a dataset comprising 600 spanwise-averaged snapshots collected over a non-dimensional temporal extent of 2.4 serves as the foundational basis for analysis.

Classical linear stability analysis

In the present study, a compressible spatial LSA is conducted to examine the stability properties of the base flow, with emphasis on the frequency response.

LSA assumes that the disturbance is linear, which is thus modelled as two-dimensional travelling waves in the shape of

$$\psi = \hat{\psi}(n)\exp[\mathrm{i}(\alpha s + \beta z - \omega t)]. \tag{4}$$

Here, s represents the arc-length from the leading edge, and the eigenfunction $\hat{\psi}(n)$ solely relys on the wall-normal coordinate n owing to a parallel assumption. Besides, β represents the real spanwise wavenumber and $\alpha = \alpha_r + \mathrm{i}\alpha_i$ is the complex streamwise wavenumber. The real component α_r specifies the streamwise wavelength $\lambda = 2\pi/\alpha_r$, while the imaginary part $(-\alpha_i)$ corresponds to the exponential spatial growth rate. In addition, ω denotes the real circular frequency, leading to the frequency $f = \omega/(2\pi)$. Substituting mean profiles and formula (4) into the linearized Navier–Stokes equations, a spatial eigenvalue problem is formulated, then $(-\alpha_i)$ is acquired by searching for the most unstable eigenvalue. Moreover, the N-factor can be numerically approximated by $N = \int_{s_0}^{s} -\alpha_i(\xi, f)\mathrm{d}\xi$, which offers a suitable estimation for the most amplified instability wave within the boundary layer (Jones *et al.*, 2010).

Forced Navier-Stokes equations

By relaxing the linear and parallel assumptions, a comprehensive analysis of the absolute and convective stability features can be conducted through DNS incorporating forcing terms, namely the forced Navier-Stokes equations (Jones *et al.*, 2010). This method is equivalent to a two-dimensional linear stability analysis, and a brief overview of the methodology is provided.

The forcing terms are represented by

$$\left.\frac{\partial}{\partial t}Q_i\right|_{t=0} = -\frac{\partial}{\partial x_j}(\overline{E}_{ji} - \overline{F}_{ji}), \tag{5}$$

where the overline signifies time- and spanwise-averaged quantities. These terms are stored at the first step and subsequently subtracted in each Runge-Kutta substep of equation (3). Thus the forced Navier-Stokes equations can be written as

$$\frac{\partial}{\partial t}Q_i = -\frac{\partial}{\partial x_j}(E_{ji} - F_{ji}) - \left.\frac{\partial}{\partial t}Q_i\right|_{t=0}. \tag{6}$$

Since the initial base flow is preserved by forcing terms, the introduction of a perturbation within the initial flow allows for an investigation of its evolution as the simulation progresses, including discerning absolute and convective stability characteristics (Jones *et al.*, 2010).

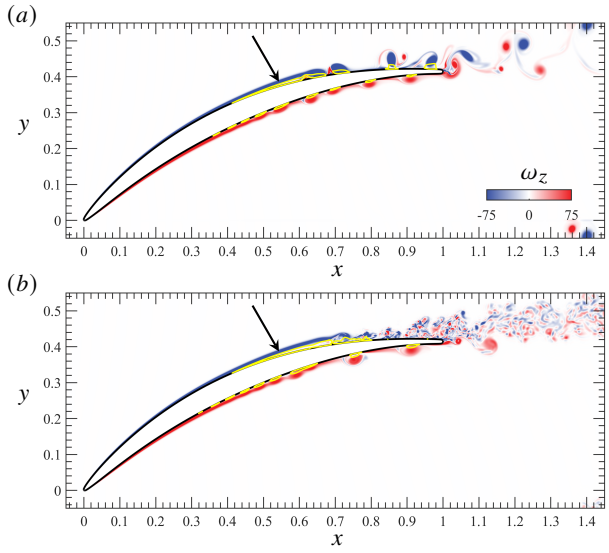

Figure 1. Instantaneous overview of the flow field of (a) case L and (b) case T, where contours of the spanwise vorticity ω_z in the cross-spanwise plane $z = 0$ are presented. Moreover, yellow lines represent the recirculation zones, and large separation bubbles are denoted by the black arrows.

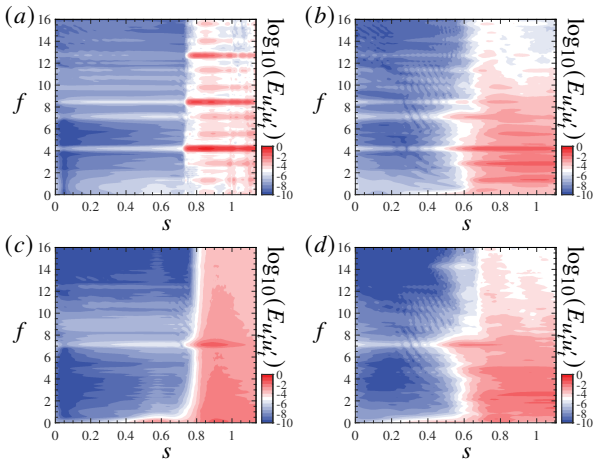

Figure 2. Frequency response $E_{u'_t u'_t}$ along the blade surface of case L on the (a) suction side and (b) pressure side, case T on the (c) suction side and (d) pressure side.

UNSTEADY FLOW FIELD ANALYSIS

Overview of the flow field

Figure 1 depicts the flow structures for both cases L and T. As shown in figure $1(a)$, case L reveals a pronounced recirculation area dominating the suction side. Divorced from its rear portion, a minor recirculation zone can be discerned, associated with the shedding of clockwise-rotating vortices. For comparison, the scenario of case T in figure $1(b)$ portrays the disintegration of the shear layer, leading to the subsequent breakdown of cohesive separation regions, indicative of the transition. Conversely, boundary layers on the pressure side in both scenarios manifest as enclosed separation bubbles.

Fluctuations within the boundary layer

Given the periodic nature of separation phenomena, we explore the frequency response within blade boundary layers. Firstly, an analysis of the frequency spectra of streamwise velocity fluctuations $E_{u'_t u'_t}$ is conducted. As illustrated in figure

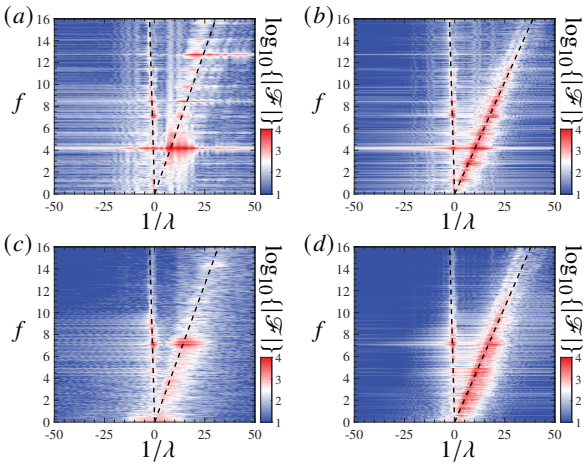

Figure 3. Fourier transform in space and in time for a pressure signal extracted of case L within the (a) suction side and (b) pressure side, case T within the (c) suction side and (d) pressure side, where log of the modulus of coefficients $\mathscr{F}$ is presented. Besides, dashed lines highlight the hydrodynamic fluctuations and sound waves.

$2(a)$, downstream the suction side of case L exhibits a pronounced periodicity when $s \geq 0.75$. The spectral analysis unveils a peak frequency at $f = 4.24$, aligning with the shedding frequency of vortices. Additionally, notable responses are detected at two- and three-fold dominant frequency, accompanied by the presence of multiple discrete frequencies. Conversely, on the pressure side, although the same dominant frequency is observed, no discrete frequencies are evident, as portrayed in figure $2(b)$. Notably, the primary energetic contributions reside in lower frequency range, attributed to the amalgamation of discrete separation bubbles. In contrast, on the suction side of case T, a singular dominant frequency is identified at $f = 7.10$, as depicted in figure $2(c)$. Besides, the absence of discrete frequencies may be linked to the boundary layer transition. Moreover, the frequence response of case T presents an analogous result to that of case L on the pressure side, as illustrated in figure $2(d)$.

Apart from velocity signals, we also investigate near-wall pressure fluctuations, which are intrinsically linked to wave propagation. Thus a frequency-wavenumber analysis is executed on the fluctuating pressure fields $p'(t, s)$, with outcomes detailed in figure 3. In each graph, there are two distinct types of waves (Desquesnes *et al.*, 2007), which are denoted by dashed lines. The first set of waves, characterized by a steep negative slope, correspond to upstream-travelling acoustic waves, owing to their proximity in speed to c_∞. Conversely, the second wave category embodies unstable convective waves propagating downstream.

Tonal noise in the near wake

The unsteadiness is further examined through the assessment of sound pressure levels (SPL) employing five strategically positioned probes in the near wakes.

As illustrated in figure $4(a)$, the SPL of case L showcases a sequence of evenly spaced discrete frequencies, inclusive of the dominant tone and its harmonics. These frequencies exhibit pronounced responses within a confined frequency band. The observed similarities between this depiction and earlier findings detailed by Desquesnes *et al.* (2007) imply that case L emits tonal noise, indicative of the presence of acoustic feedback. In contrast, as depicted in figure $4(b)$, the SPL in case T presents

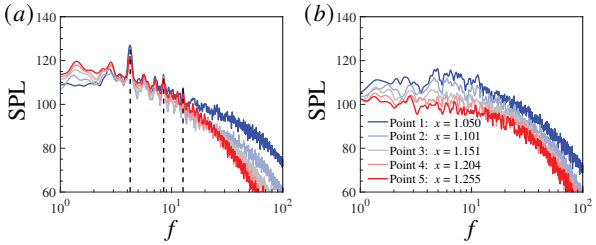

Figure 4. SPL calculated from five probes located in near-wakes of (a) case L and (b) case T. For case L, the dominant tone and its multipliers are marked.

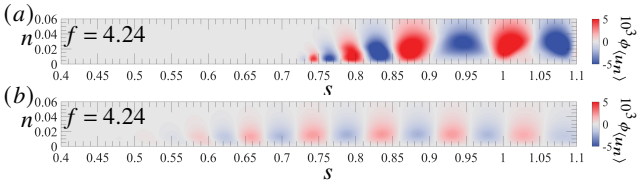

Figure 5. The dominant DMD mode of case L on the (a) suction side and (b) pressure side.

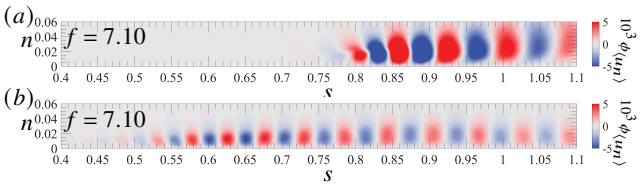

Figure 6. The dominant DMD mode of case T on the (a) suction side and (b) pressure side.

a turbulent state devoid of distinct discrete frequencies, thus negating the existence of tonal noise.

Dynamic mode decomposition analysis

Given the presence of self-sustained oscillations, a global mode is inferred to exist (Jones *et al.*, 2010; Fosas de Pando *et al.*, 2014), thus the DMD technique is employed.

Focusing on the spanwise-averaged normal velocity component $\langle u_n \rangle$, two cases unveil significantly different dominant frequencies, with corresponding spatial configurations elucidated in figures 5 and 6. Roughly speaking, patterns representing unstable hydrodynamic waves are observed to emerge from the unsteadiness commencement in both the suction and pressure sides, indicating that the dominant mode originates from separation events.

HYDRODYNAMIC INSTABILITY ANALYSIS

Classical linear stability analysis

To delve deeper into the intricate flow dynamics, a local stability analysis is employed to scrutinize the instability mechanisms, with a particular focus on the N-factor.

Approximating the dominant frequency closely, the selection of the most unstable frequency is typically predetermined before the inception of unsteadiness, as indicated by dashed black lines in figure 7. The encirclements depicted in figures $7(a)$ and $7(c)$ indicate that the frequency corresponding to the peak closely aligns with the separation frequency observed in case T, presenting a stark contrast to the characteristics exhibited in case L. Further scrutiny of figures $7(b)$ and $7(d)$ exposes a convergence of unstable modes on the pressure side towards $f = 7.10$ prior to separation. It seems that the dominant frequency at $f = 7.10$ for case T is presumably induced by the boundary layer instability, while the frequency responses for case L are governed by other mechanisms.

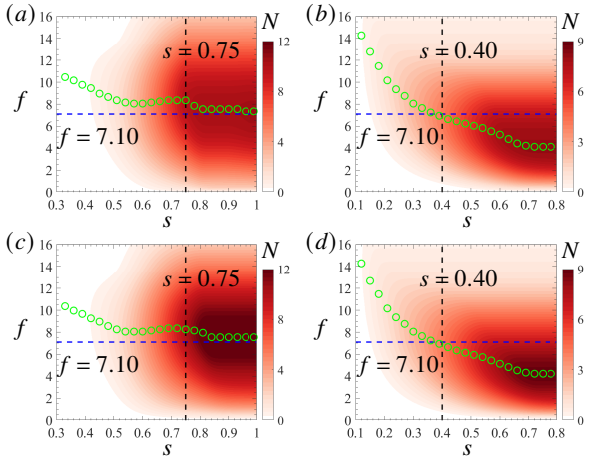

Figure 7. Spatial stability analysis results of case L on the (a) suction side and (b) pressure side, case T on the (c) suction side and (d) pressure side, where contours of the N-factor are displayed. Here, green circles mark the maximum N-factor at different streamwise locations, and dashed black lines indicate the inception of unsteadiness.

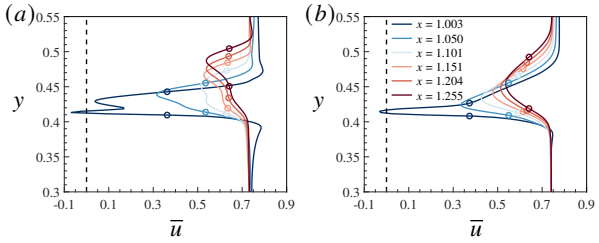

Figure 8. Velocity deficit profiles in the near-wakes of (a) case L and (b) case T. Here, circles mark the half-width locations of wakes, and dashed black lines represent $\overline{u} = 0$.

Near-wake instability

In addition to boundary layer instability, our investigation extends to the study of near-wake instability, aimed at unraveling the origins of the dominant mode.

Figure 8 shows mean profiles of the horizontal velocity $\overline{u}$, where local reverse flow suggests the potential influence of the near-wake instability (Ikeda *et al.*, 2012). Based on the minimum half-width $b_{\min}$, Tam & Ju (2012) claimed that the most amplified frequency can be well-characterized by a fitting of $2\pi f b_{\min}/U_\infty \approx 0.43$. For case L, the predicted value $f \approx 4.12$ agrees with the dominant tone observed in figure $4(a)$, albeit notably lower than the estimation from LSA. This discrepancy suggests that the dominant frequency being predominantly governed by the near-wake instability. Conversely, given the absence of prominent tones in case T as depicted in figure $4(b)$, the near-wake instability appears not to be the primary mechanism in this instance.

TWO-DIMENSIONAL LINEAR STABILITY ANALYSIS

Convective and absolute instabilities

Through forced Navier-Stokes simulations, stability traits and emergent acoustic behaviours are investigated by monitor-

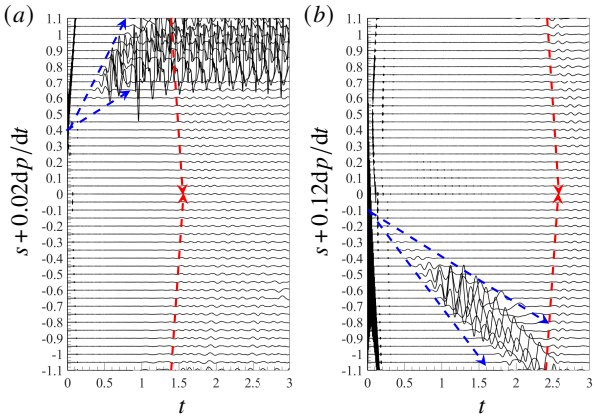

Figure 9. Time histories of $\mathrm{d}p/\mathrm{d}t$ of forced case L, with the initial impulse are introduced at (a) $s = 0.4$ and (b) $s = -0.1$. Here, negative streamwise location s denotes the pressure side, while positive s denotes the suction side. Besides, dashed blue arrows indicate the propagation of the initial disturbances, and dashed red arrows mark the scattering waves from the trailing edge.

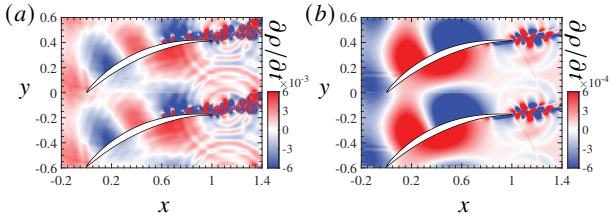

Figure 10. Acoustic source near the trailing edge for forced case L, which is shown by contours of $\partial\rho/\partial t$. Here, the initial impulse are introduced on the (a) suction side at $s = 0.4$ and (b) pressure side at $s = 0.1$.

ing the evolution of signals, as depicted in figure 9. Here, only results obtained from the mean flow of case L are exhibited, since case T give the same conclusions.

As illustrated in figure 9(a), upon the introduction of stimulation on the suction side, a sustained disturbance downstream suggests the presence of absolute instability within the suction-side boundary layer (Huerre & Monkewitz, 1990). In contrast, as depicted in figure 9(b), when the stimulation is applied on the pressure side, the flow ultimately reverts to an undisturbed state, indicative of the convective instability. Furthermore, as the initial disturbance pasts the trailing edge, the emergence of an upstream-travelling acoustic wave emphasized by red lines signifies the phenomenon of trailing-edge scattering.

Trailing-edge scattering

The stimulation on the suction side results in a sustained perturbation marked by vortex shedding, demonstrating attributes of absolute instability, as shown in figure 10(a). Concurrently, an array of annular acoustic waves incessantly emanates in the vicinity of the trailing edge. In contrast, owing to the convective instability, there is only one conspicuous acoustic wave emerging, and the snapshot is captured in figure 10(b). These findings underscore the presence of trailing-edge scattering, with acoustic feedback predominantly governed by the suction side.

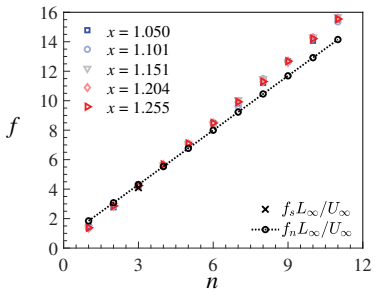

Figure 11. Discrete frequencies in the near-wake and predictions of the acoustic feedback's model based on formulas (1) and (2), which are nondimensionalized with reference quantities of L_∞ and U_∞.

Acoustic feedback loop

Based on the above-mentioned discussion, the concrete acoustic feedback loop can be summarized as: unstable waves originated from the unsteady separation progress downstream and ultimately traverse the trailing edge. This sequential process gives rise to the generation of acoustic waves through scattering phenomena, leading to their omnidirectional radiation. Subsequent interactions between the generated acoustic waves and the downstream-traveling unstable waves engender the establishment of a robust acoustic feedback loop primarily driven by the absolute instability, resulting in the emergence of equidistant discrete frequency components. The graphical representation provided in figure 11 exhibits a consonance between the observed discrete frequencies and the analytical predictions derived from equations (1) and (2), thereby substantiating the proposed theoretical framework.

SELF-SUSTAINING TURBULENCE

Furthermore, we undertake an investigation to elaborate the absence of tonal noise in case T, which is probably due to the chaotic phase of pressure fluctuations caused by three-dimensional structures (Gelot & Kim, 2020). Commencing with case L, a stochastic disturbance is seed at $s = 0.4$ on the suction side, spanning across the spanwise domain, and the resulting transitional structures are focused on.

Under the influence of absolute instability, the coherent spanwise structures of vortices identified by the Q-criterion (Hunt *et al.*, 1988) gradually undergo a distortion over temporal evolution. As presented in figure 12, both Λ-shaped and hairpin-like vortices are discernible, emblematic of transition phenomena. Additionally, iso-surfaces of scaled streamwise vorticity ω_t^* exhibit intricate patterns, showcasing alternating sign regions within and enveloping the vortices, characterized by spanwise-periodic variations. The spanwise wavelength $\lambda_z = L_z/3 \approx 0.67$ approximately aligns with the core dimension of the vortices $D = 0.5 \sim 0.6$, hinting at a probable association with mode-B instability dynamics (Williamson, 1996).

CONCLUSIONS

Two three-dimensional DNS simulations are performed for the flow in a compressor cascade in the present study, one is an laminar case namely case L, and the other refers to case T. Employing DMD and LSA techniques, as well as forced Navier-Stokes simulations, we concentrate on the frequency response and underlying instability mechanisms.

The suction-side boundary layer is characterized as shedding separation, while the pressure side is manifested as closed

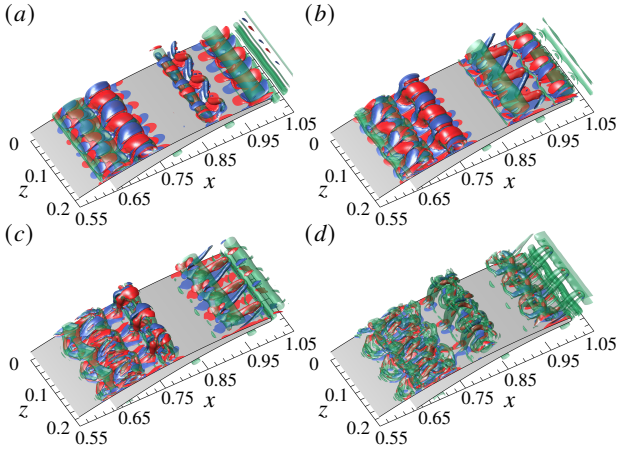

Figure 12. Flow structures undergoing the transition taken at four phases of the vortex shedding cycle, where the initial impulse are introduced on the suction side at $s = 0.4$. Here, red iso-surfaces represent $\omega_t^* = 0.5$, while blue iso-surfaces represent $\omega_t^* = -0.5$. The vortical structures are presented by the green iso-surfaces of $Q = 500$.

separation bubbles. Noteworthy is the manifestation of multiple frequencies detected on the suction side within case L, concomitantly discernible within the PSD analysis in the near wake region. Nevertheless, case T undergoing a transition only reveals a single frequency, coupled with turbulent behavior within the near wake region. Moreover, dominant frequencies of two cases are different. Within case L, the frequency response on the suction side is attributed to the acoustic feedback occurring between the inception of unsteady separation and the trailing edge, with the dominant tone further selected by the near-wake instability. Conversely, a self-sustained turbulence occurs in case T due to the mode-B instability weakens the feedback loop. Affected by boundary layer instability, a single dominant frequency manifests in case T, which is different from that in case L and can be predicted by the LSA method.

ACKNOWLEDGMENTS

T. Wang and Y. Zhao were supported by the National Natural Science Foundation of China (Grant Nos. 92152102 and 92152202), and the Advanced Jet Propulsion Innovation Center/AEAC, funding number HKCX2022-01-010. The code for the compressible spatial linear stability analysis was kindly provided by D. Sun, and we thank M. She for helpful instructions. Besides, we also thank B. Lyu for enlightening discussions on acoustic phenomena.

REFERENCES

Arbey, H. & Bataille, J. 1983 Noise generated by airfoil profiles placed in a uniform laminar flow. *J. Fluid Mech.* **134**, 33–47.

Arcondoulis, Elias, Doolan, Con J., Zander, Anthony C., Brooks, Laura A. & Liu, Yu 2019 An investigation of airfoil dual acoustic feedback mechanisms at low-to-moderate reynolds number. *J. Sound Vibr.* **460**, 114887.

Desquesnes, G., Terracol, M. & Sagaut, P. 2007 Numerical investigation of the tone noise mechanism over laminar airfoils. *J. Fluid Mech.* **591**, 155–182.

Fink, Martin R. 1975 Prediction of airfoil tone frequencies. *J. Aircraft* **12** (2), 118–120.

Gelot, Matthieu B. R. & Kim, Jae Wook 2020 Effect of serrated trailing edges on aerofoil tonal noise. *J. Fluid Mech.* **904**, A30.

Huerre, P & Monkewitz, P A 1990 Local and global instabilities in spatially developing flows. *Ann. Rev. Fluid Mech.* **22** (1), 473–537.

Hunt, J. C. R., Wray, A. A. & Moin, P. 1988 Eddies, streams, and convergence zones in turbulent flows. In *Studying Turbulence Using Numerical Simulation Databases, 2*, , vol. 1, pp. 193–208. Center for Turbulence Research Report CTR-S88.

Ikeda, Tomoaki, Atobe, Takashi & Takagi, Shohei 2012 Direct simulations of trailing-edge noise generation from two-dimensional airfoils at low reynolds numbers. *J. Sound Vibr.* **331** (3), 556–574.

Jones, L. E., Sandberg, R. D. & Sandham, N. D. 2008 Direct numerical simulations of forced and unforced separation bubbles on an airfoil at incidence. *J. Fluid Mech.* **602**, 175–207.

Jones, L. E., Sandberg, R. D. & Sandham, N. D. 2010 Stability and receptivity characteristics of a laminar separation bubble on an aerofoil. *J. Fluid Mech.* **648**, 257–296.

Longhouse, R.E. 1977 Vortex shedding noise of low tip speed, axial flow fans. *J. Sound Vibr.* **53** (1), 25–46.

Mao, X., Zaki, T. A., Sherwin, S. J. & Blackburn, H. M. 2017 Transition induced by linear and nonlinear perturbation growth in flow past a compressor blade. *J. Fluid Mech.* **820**, 604–632.

Nash, Emma C., Lowson, Martin V. & Mcalpine, Alan 1999 Boundary-layer instability noise on aerofoils. *J. Fluid Mech.* **382**, 27–61.

Fosas de Pando, Miguel, Schmid, Peter J. & Sipp, Denis 2014 A global analysis of tonal noise in flows around aerofoils. *J. Fluid Mech.* **754**, 5–38.

Paterson, Robert W., Vogt, Paul G., Fink, Martin R. & Munch, C. Lee 1973 Vortex noise of isolated airfoils. *J. Aircraft* **10** (5), 296–302.

Pauley, Laura L., Moin, Parviz & Reynolds, William C. 1990 The structure of two-dimensional separation. *J. Fluid Mech.* **220**, 397–411.

Pröbsting, S., Scarano, F. & Morris, S. C. 2015 Regimes of tonal noise on an airfoil at moderate reynolds number. *J. Fluid Mech.* **780**, 407–438.

Sandberg, Richard D. & Michelassi, Vittorio 2022 Fluid dynamics of axial turbomachinery: blade- and stage-level simulations and models. *Ann. Rev. Fluid Mech.* **54**, 255–285.

Sandberg, Richard D, Michelassi, Vittorio, Pichler, Richard, Chen, Liwei & Johnstone, Roderick 2015 Compressible direct numerical simulation of low-pressure turbines-Part I: Methodology. *ASME J. Turbomach.* **137**, 051011.

Schmid, Peter J. 2010 Dynamic mode decomposition of numerical and experimental data. *J. Fluid Mech.* **656**, 5–28.

Tam, Christopher K. W. 1974 Discrete tones of isolated airfoils. *J. Acoust. Soc. Am.* **55** (6), 1173–1177.

Tam, Christopher K. W. & Ju, Hongbin 2012 Aerofoil tones at moderate reynolds number. *J. Fluid Mech.* **690**, 536–570.

Williamson, C H K 1996 Vortex dynamics in the cylinder wake. *Ann. Rev. Fluid Mech.* **28** (1), 477–539.

Zaki, Tamer A., Wissink, Jan G., Rodi, Wolfgang & Durbin, Paul A. 2010 Direct numerical simulations of transition in a compressor cascade: the influence of free-stream turbulence. *J. Fluid Mech.* **665**, 57–98.